Simultaneous Measurements of Mixing Fraction and Velocities of a Coaxial Jet in a Turbulent Channel Flow

Joachim Klinner*,[1], Valentin Mayer[2], Johannes Heinze[1], Christian Willert[1]

1: Institute of Propulsion Technology, German Aerospace Center (DLR), 51170 Köln, Germany
2: Daimler AG, D-70546 Stuttgart, Germany
*correspondent author: joachim.klinner@dlr.de

Abstract Simultaneous velocity and concentration measurements of the isothermal mixing of a confined coaxial jet in air are performed in a small scale windtunnel at ambient conditions. The Reynolds number is 26000 based on the velocity difference of streams and on the diameter of the injection port. Instantaneous concentration measurements are implemented using planar laser induced fluorescence (PLIF) of acetone seeded injected flow. Simultaneous three-component velocity measurements are performed using stereo particle image velocimetry (PIV). The contribution provides details of the PLIF-PIV measurement setup and of the methodology to obtain instantaneous measurements of the local mixing fraction and velocity. Ensemble averaged velocities, concentrations, Reynolds stresses and turbulent mass fluxes are determined at four positions downstream of the nozzle using up to 3600 PLIF-PIV recordings. The convergence of the root-mean-square of velocity and concentration measurements is assessed in exemplary regions within the shear layers of the mixing zone. The recovered profiles of ensemble averaged velocity, Reynolds stresses and turbulent mass fluxes are compared to Reynolds averaged Navier-Stokes (RANS) and scalar transport simulations. Accompanying RANS calculation of the flow exhibit a strong underestimation of mixing and diffusion rates which can be attributed to the strong anisotropic behavior of this flow.

1. Introduction

The present investigation is motivated by the performance assessment of established numerical methods with regard to prediction of turbulent scalar transport and mixing. In particular the optimization of exhaust gas recirculation and urea injection for NOx-reduction in internal combustion engines requires a detailed knowledge of mixing processes of the engines' gas, oxygen, fuel and additives. The spatial and temporal distribution of reactants upstream of the mixing port can be significantly affected by turbulent transport. The optimization of the reactor and mixing port geometry by computational fluid dynamics (CFD) requires experimental data to validate turbulent transport models.
This contribution describes a generic mixing experiment aimed at providing experimental data of turbulence induced mass transfer to validate Reynolds averaged Navier-Stokes (RANS) and Reynolds-averaged scalar transport simulations. The focus is not only on average quantities of velocity and concentration but on turbulent fluctuations and the degree of correlation of these fluctuations. The latter is represented by Reynolds stresses and turbulent scalar fluxes $u_i'c'$ in the scalar transport equation. The turbulent mass flux vector describes both the direction and the magnitude of the mass transport by turbulence. In order to estimate the steady-state turbulent mass flux vector $\langle u_i'c' \rangle$, simultaneous measurements of velocity and mixing fraction at high spatial resolution are required to obtain statistical information on the covariances between velocity and concentrations.
The measurements are performed in a small scale wind tunnel as outlined in Fig. 1. The wind tunnel is operated in suction mode. The mixing port is placed at a third of the test section length and consists of a 90° bend.
Instantaneous concentration measurements are implemented using planar laser induces fluorescence (PLIF) of the acetone seeded injected flow following the work of Lozano et al [1992], Bryant et al [2000], Thurber et al [1998]. Simultaneous velocity measurements are performed using particle image

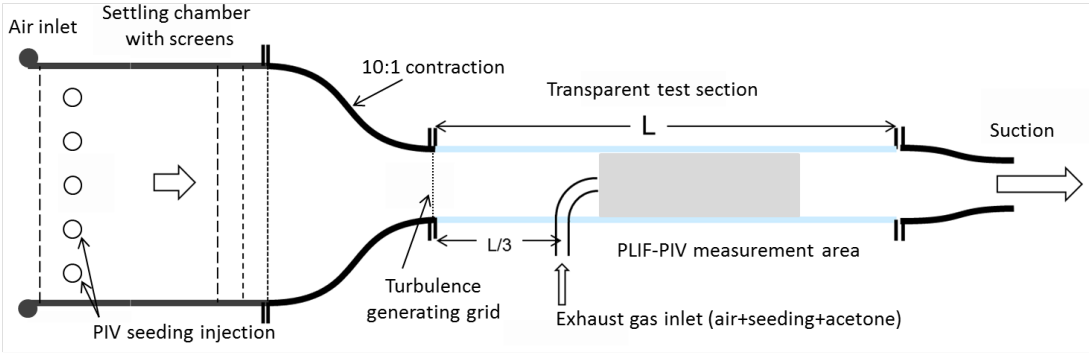

Fig. 1: Schematic diagram of wind tunnel facility with approximate location of acetone PLIF and PIV measurement area

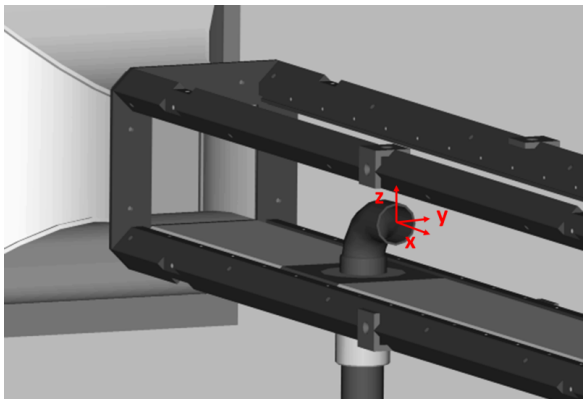

Fig. 2 3D view of the test section and orientation of the coordinate system

velocimetry (PIV) where out of plane components are measured using a second double frame camera in stereoscopic arrangement [Prasad, 2000].
Ensemble-averages of velocity, mixing fraction, Reynolds stresses and turbulent mass flux are determined at four positions downstream of the nozzle using sets of up to 3600 PIV recordings. The convergence of the root-mean-square of velocity and concentration measurements over N is assessed in exemplary regions within the shear layers of the mixing zone. The measurement uncertainty of each velocity component is estimated from the stereo PIV viewing arrangement and statistical uncertainties of displacement detection. The uncertainty of PLIF measurements are discussed in terms of statistical and systematical errors.
The recovered profiles of ensemble-averaged velocity, concentration, Reynolds stresses and turbulent mass fluxes are compared to corresponding RANS simulations using a variety of "state of the art" turbulence models in an effort to assess their performance in predicting the mixing processes. The present work has been carried out using STARCCM+ which has the capabilities to handle complex geometry and exhibit multi-physics solver. STARCCM+ [Starccm [2013]] is a computational fluid dynamics (CFD) code based on finite volume method with second-order accuracy in space. It uses cell-based discretization techniques and advanced algebraic-multi-grid(AMG) strategies.

2. Flow facility and operating conditions

The wind tunnel (see Fig. 1) is operated in suction mode and has a 830 mm long test section with a square cross-section of internal width of 76 mm. Quartz windows with 45° edge bevels provide optical access to the entire cross-section. As outlined in Fig. 1 flow conditioning is provided by a settling chamber containing screens and straightening tubes. Reproducible turbulent flow conditions within the test section are provided by a turbulence grid made of perforated steel that is placed immediately

Tab. 1: Flow paramter

	Symbol	Tunnel inlet	Injection inlet	Tunnel Outlet	Units
Position	x	-110	0	200	mm
Mass flow	$\dot{m}$	22.5	11.5	34	g/s
Hydraulic diameter	D (tunnel), d (nozzle)	76	25	76	mm
Bulk velocity	u_0	3.25	19.5	4.9	m/s
Reynolds number based on d,D and u_0	Re	16250	32000	24500	
Friction velocity at upper wall	u_τ	0.199	0.181	0.265	m/s

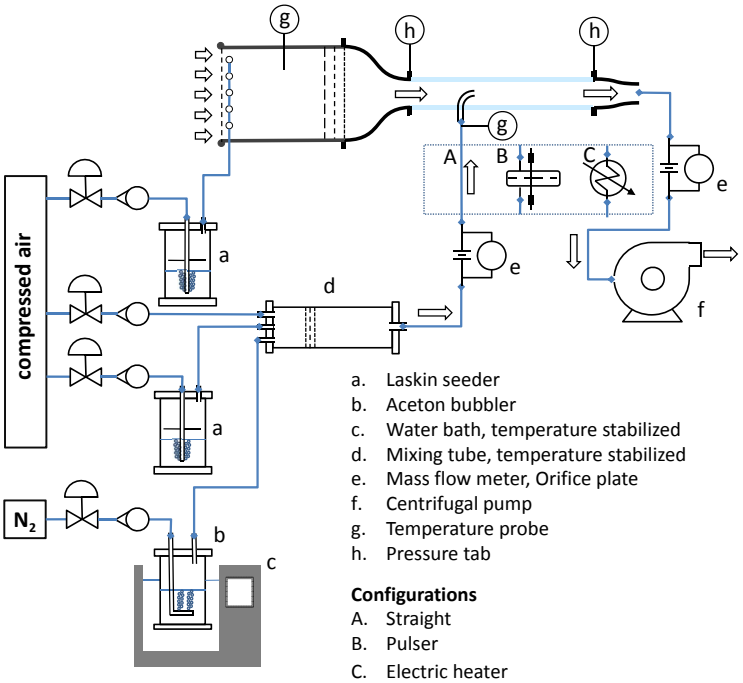

Fig. 3 Flow chart and instrumentation of the wind tunnel, the straight configuration (A) is used for experiments presented here

upstream of the test section at the exit of contraction nozzle. The turbulent fluctuations of the main flow immediately upstream of the mixing port have decayed to levels of Tu=0.02 which is verified by planar PIV measurements at center plane. The mixing port is placed at a third of the test section length and consists of a 90° bend. The inner tube diameter is 25 mm with the bend exit aligned coaxially to the channel's center line.

Flow parameters of tunnel inlet, injection inlet and tunnel outlet are provided in table 1. The exhaust gas flow is injected into the tunnel flow at approximately half mass flow rate. The Reynolds number of the incoming main flow of the tunnel is 16000 and the Reynolds number of the injected air is 32000, both of which are based on bulk velocities and hydraulic diameter. The Reynolds number is 26000 based on the velocity difference of both streams and on the diameter of the injection port. The momentum flux ratio is 30 at the exit of the 90° bend, based on bulk velocities. The friction velocities u_τ at both inlets given in table 1 are obtained from long PIV sequences of the viscous sublayer reported in Willert [submitted]. The friction velocity at tunnel outlet is based on the model of a flat plate and the pressure difference from pressure tabs at tunnel inlet and outlet.

The flow chart in Fig. 3 shows the instrumentation of the windtunnel air supply and suction system as well as the PIV seeding and acetone supply. Orifice plates are used to monitor the suction and injection mass flow rates. During long PLIF-PIV acquisition runs (12 minutes, 3600 images at 5Hz

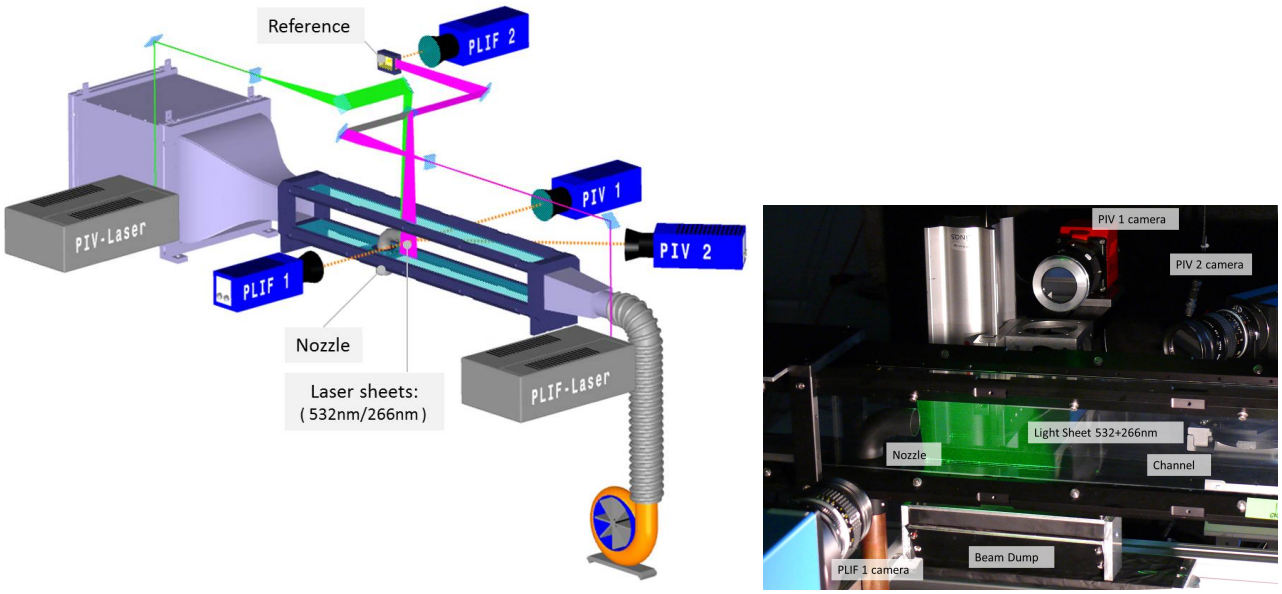

Fig. 4: Schematic of the combined PLIF-PIV setup and imaging setup

frame rate) the suction mass flow is stable to within $\pm 0.4\%$ and the injected mass flow is stable to within $\pm 0.2\%$ related to the mean mass flow rates. The nitrogen mass flow through the bubbler is enriched with acetone tracer gas to initial volume concentration levels of approximately 40 vol% . The estimation of this initial concentration is based on the saturation vapor pressure of acetone taken from Lozano et al [1992] at a water bath temperature of $35°$. The initial concentration is further diluted to levels of 0.5 vol% tracer gas concentration at the injection inlet. The acetone bubbler, the mixing tube and the acetone supply lines upstream of the mixing tube are temperature stabilized to avoid acetone condensation and to keep the acetone tracer concentration stable during the long runs. In order to minimize variations of optical quenching due to differences of gas compositions between the injection flow and the mean flow, the nitrogen supply to the acetone bubbler is limited to low mass flow rates amounting to about 1.4 vol% of the injected mass flow rate.

3. Combined acetone PLIF and PIV setup

The optical setup of combined PLIF-PIV measurements is depicted in Fig. 4. The windtunnel is mounted on a x-y translation stage to enable measurements in different regions while the PLIF-PIV setup remains at a fixed position. The measurement results within this contribution are obtained at the channel x-z center plane and are measured in the mixing zone between x=0-300 mm equivalent to 0-12 nozzle diameters. Measurements at the large field-of-view of $110 \times 76\,\mathrm{mm}^2$ are acquired to obtain an overview of the average velocity and concentration field. In order to evaluate statistical fluctuations of velocity and concentration up to 3700 single shot measurements are acquired in small regions of $20 \times 76\,\mathrm{mm}^2$.
Measurements of instantaneous concentration are achieved using planar laser induced fluorescence (PLIF) of the acetone seeded injection flow. Acetone has a wide absorption spectrum between 200 and 325 nm [Lozano et al, 1992] and is excited with a quadrupled Nd:YAG pulse laser at 266 nm. The laser has a pulse energy of 80 mJ and a pulse width of 12 ns (Quanta Ray, Spectra Physics). The laser beam is converted into a divergent light sheet of 80μm thickness which has a height of 120 mm at windtunnel's centerline. With excitation at 266 nm the spectral range of the prompt acetone fluorescence extends from 320...600 nm [Bryant et al, 2000; Tran et al, 2005]. Fluorescence images are acquired with an intensified camera (Dicam Pro, PCO AG) equipped with a S20Q photocathode

and a Nikkor 50/$f_{\#}$1.2 lens. A short pass edge filter with a 65% cut off wavelength of 500 nm is placed in front of the lens to protect the camera from scattered light of PIV laser light at 532 nm. The camera's photocathode is gated at 40 ns centered at the laser pulse. The intensifier's gain is set to 20-30%. The intensified camera pixels are binded by 2×2 pixel which approximately matches the MCP resolution and increases the signal yield. This leads to a final magnification of 6 pixel/mm .
Simultaneous recording of the PLIF Laser sheet intensity profile allows a calibration of temporal and spatial fluctuations of the excitation energy distribution in the PLIF light-sheet as described in Heinze et al [2011]. Using a beam splitter plate, 4% intensity of the PLIF laser sheet are guided to a reference cell filled with a rhodamine 6G ethanol mixture. Permanent recycling of the fluid using a circulation pump and a reservoir avoids degradation of the dye (bleaching). The green fluorescence of the dye is observed with a CCD camera (PCO.1600, PCO AG). The images are further processed to extract the excitation intensity profile used for intensity normalization. The complete PLIF image processing chain is outlined in sect. 4. .
Simultaneous 2-C velocity measurements are obtained using particle image velocimetry (PIV) in a normal viewing arrangement (ILA.sCMOS.PIV, ILA GmbH). The camera is equipped with a Zeiss 85/$f_{\#}$2 lens and observes the field of view at a magnification of approximately 22 pixel/mm . Out of plane components in the wake of the 90° bend are measured with stereo PIV [Prasad, 2000] using a second double frame camera under 30° viewing angle (pco.2000, PCO AG). The second PIV camera is equipped with a Nikkor 55/$f_{\#}$2.8 macro lens at approximately the same magnification as the sCMOS. Bandpass filters with a spectral width of 10nm and a center wavelength of 532 nm reject stray light. Both, the inlet flow and the injected flow are seeded at matching tracer concentrations. The seeding consists of paraffin aerosol created by two Laskin atomizers Fig. 3. Impactors in the seeding device reduce the size fraction below 1 μm prior to introducing the seeded air respectively to the settling chamber and mixing tube. The paraffin tracer droplets are illuminated using a doubled Nd:YAG laser with a rated pulse energy of 50 mJ (Brilliant Twins, Quantel/BigSky Laser). The fluorescence of paraffin droplets at excitation of 266 nm was found to be of little insignificance in comparison of the acetone fluorescence. The droplet fluorescence increased averaged background levels of PLIF measurements of 100 counts by 10% while the maximum acetone fluorescence is in the order of 2000 counts and more.
Trigger pulses for all lasers and cameras are generated by a programmable timing generator (PIVseqPCI, PIVTEC GmbH). The acquisition rate of combined measurements is 5 Hz which is a compromise of having all lasers operating at optimum flash lamp repetition rates (10 and 15 hz) while all Q-switches fire at a common frequency. The pulse separation Δt was set between 25...35 μs according to displacement PDFs to have an average particle image displacement of 10 pixel and validation rates of better than 75% in the shear layers. The timing of a single PLIF-PIV measurement was chosen in such a way that the Q-switch of the PLIF laser fires always at Δt /2.

4. PLIF image evaluation

Following the the work of Coppeta and Rogers [1998] and Bryant et al [2000] the planar fluorescence signal at an arbitrary point p in the light sheet is given by

$$S_f(p) = I_e(p)\, C(p)\, \epsilon\, \Phi\, L(p)\, A(p)\, G \tag{1}$$

where S_f is the measured fluorescence intensity at p, I_e is the intensity of the excitation light beam at p, A is the fraction of fluorescence light collected by the lens, G is the camera gain , Φ is the quantum efficiency, L is the length of the sampling volume along the path of the excitation beam, ϵ is the molar absorptivity, and C is the molar concentration of the fluorophor at p. The linear dependency of the fluorescence signal and the acetone tracer concentration is only given if the energy flux in the light sheet is below the saturation level and absorption is neglected. Bryant et al [2000] reported a linear

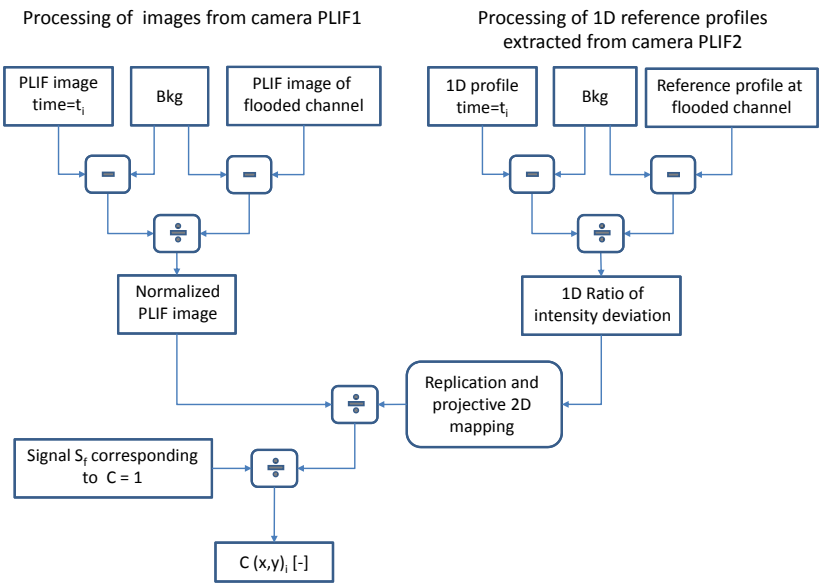

Fig. 5 Processing of PLIF images and 1D profiles of laser intensity obtained from the reference camera

response of acetone vapor at a maximum energy flux of 353 mJ/cm^3 when excited at 266 nm (10 ns pulse width) under ambient conditions. Lozano et al [1992] reported a linear response at a maximum energy flux of 1140 mJ/cm^3 when excited at 313 nm (20 ns pulse width). The maximum laser energy flux in the experiment is 500 mJ/cm^3 at 12 ns pulse duration. The linearity of the signal was verified prior measurements and no evidence of saturation was found.

The acquired PLIF images are first flat-field corrected according to the procedure depicted in Fig. 5. After background subtraction, images are divided by a sensitivity image. The sensitivity image is recorded while the channel is flooded with a homogeneous acetone tracer concentration (average over 200 images). This procedure accounts for the angular lens collection efficiency A, variations of sensitivity of the camera, the quantum efficiency of fluorescence and spatial variations of laser intensity. In order to correct for additional shot-to-shot fluctuations, each single image at t_i is corrected according to laser profile deviations at the same time. This profile is extracted from reference images of the rhodamine cell. The profile is averaged along 10 pixel in propagation direction. The further proceeding of 1D profiles is as follows:

1. division by the reference profile recorded at flooded channel,
2. replication of 1D profile along image height,
3. mapping according to sheet propagation in the test section.

The mapping consists of a projective transformation using four point correspondences between reference and signal image. Point correspondences are found by calibration images of a striped light sheet. Fig. 6 shows an exemplary PLIF evaluation with and without correction of shot-to-shot intensity variations. Without this correction the mixing fraction shows inhomogeneous values and a wavy intensity distribution in the jet core (Fig. 6, left).

Fig. 7 shows the stability of the signal of maximum acetone concentration $S_{\max}$ within a rectangular region immediately downstream of the injection inlet during a run of 12 minutes. The acetone fluorescence slightly fluctuates within the first 800 measurements and remains stable throughout the remainder of the sequence with a 2.3% standard deviation from the average. The signal $S_{\max}$ is used to scale PLIF images to maximum concentration and is directly obtained from single-shot images if the injection inlet is in the field. If the injection inlet is outside the field of view $S_{\max}$ values are acquired prior and after each measurement and then linearly interpolated.

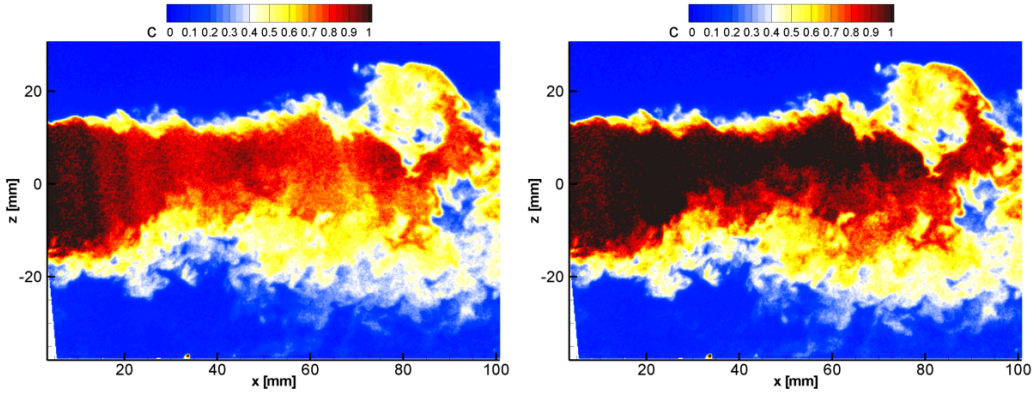

Fig. 6: Single shot results without correction (left) of shot-to-shot intensity variations in the light sheet and with correction (right). The left image clearly shows artifacts due to a wavy intensity distribution in the light sheet

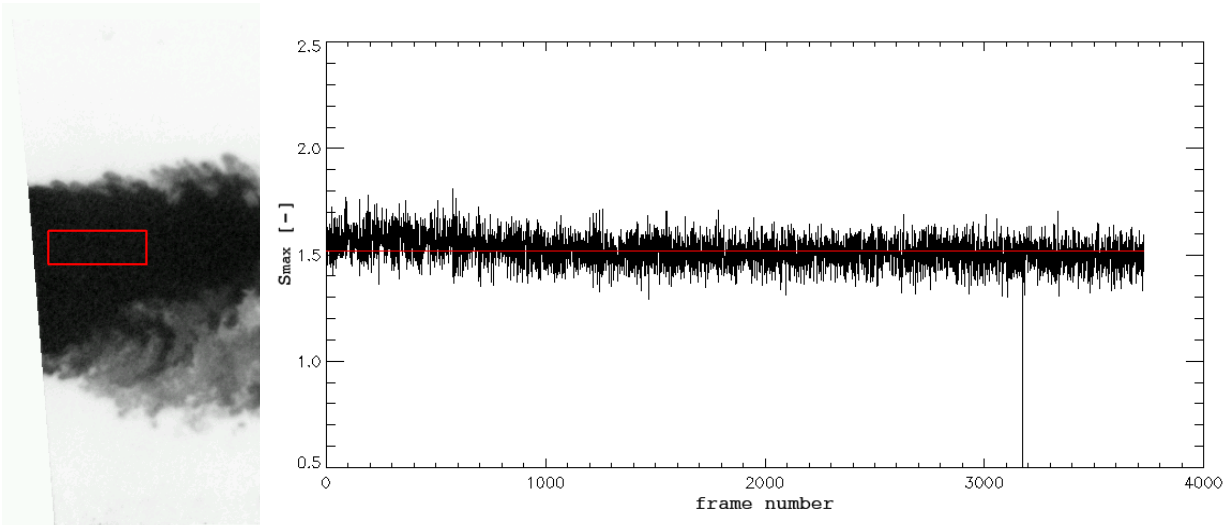

Fig. 7: Stability of the fluorescence at maximum acetone concentration immediately downstream of the injection inlet in the highlighted rectangular region. 3600 frames correspond to an acquisition time of 12 min

5. Evaluation of particle image displacements and accuracy

Stereo PIV image data is processed using PIVview 3.5.9 (PIVTEC GmbH) for which the PIV evaluation parameters are summarized in table 2. After image contrast enhancement by background subtraction each PIV double image is mapped onto a common image plane using a projective transformation based on ratios of first and second order polynomials [Raffel et al, 2007]. The image offset due to the oblique viewing of camera 2 through the window (calibration images are recorded without the window) is corrected using a disparity correction based on linear interpolation. Particle displacements are recovered using a coarse-to-fine multi-grid processing scheme with image deformation at each step to take into account the strong shear in the flow. The sub-pixel correlation peak position measurement was performed by a truncated sinc signal reconstruction algorithm. Due to this processing and a sufficient particle image density an accuracy of correlation peak detection below ± 0.1 pixel can be obtained for regions without strong laser background and without strong velocity gradients [Raffel et al, 2007]. Table 3 summarizes estimates of the accuracy of velocity obtained from SPIV viewing geometry ($\alpha_1 = 0°$ and $\alpha_2 = 30°$) based on an conservatively estimated accuracy of peakdetection of $\sigma_{2c} = 0.1$ pixel and on error propagation [Prasad, 2000]. Peak locking effects are partially observed

Tab. 2: PIV evaluation parameters

Field of view	116×80 (overview) 19×80 (statistics)	mm
	2560×1760 (overview) 420×1760 (statistics)	pixel
Magnification	22.0	pixel/mm
Pulse delay	25 - 35	μs
Window size	2.18×1.45	mm
	48×32	pixel
Sampling	1.09×0.73	mm
	24×16	pixel
Interrogation method	Multi-grid + Image deformation	
Peak detection	Whittaker reconstruction	
Vector validation test	max. displacement diff. (10 pixel),normalized median (6)	

in the displacement PDFs from PIV camera 2 and could be reduced by slightly blurring the particle images by defocussing the lens.

Tab. 3: Uncertainty of SPIV velocity components based on a peak detection accuracy of $\sigma_{2c} = 0.1$ pixel ; normalized values are related to friction velocity at tunnel outlet (see table 1)

		Injection inlet $\Delta t = 25\ \mu$s		Mixing zone $\Delta t = 30\ \mu$s		Tunnel outlet $\Delta t = 35\ \mu$s	
	σ_{3c} [pixel]	σ_{3c} [m/s]	σ_{3c}/u_τ [-]	σ_{3c} [m/s]	σ_{3c}/u_τ [-]	σ_{3c} [m/s]	σ_{3c}/u_τ [-]
u	σ_{2c}	0.18	0.69	0.15	0.57	0.13	0.49
v	$3\sqrt{2}/\sqrt{3}\,\sigma_{2c}$	0.45	1.68	0.37	1.40	0.32	1.20
w	$1/\sqrt{2}\,\sigma_{2c}$	0.13	0.49	0.11	0.40	0.09	0.35

6. Numerical method and boundary condition

In order to compare the time averaged measured data with numerical predictions, three-dimensional steady-state simulations are performed using Reynolds averaged Navier-Stokes (RANS) equations. Beside the continuity and RANS equations, the mass transfer is obtained by an additional equation [Fox, 2003]

$$\frac{\partial \langle C \rangle}{\partial t} + U_i \frac{\partial \langle C \rangle}{\partial x_i} = \frac{\partial}{\partial x_i} \left(\frac{\nu}{Sc} \frac{\partial \langle C \rangle}{\partial x_i} - \langle u_i' c' \rangle \right). \tag{2}$$

The turbulent mass flux $\langle u_i' c' \rangle$ is modeled by the widely used gradient hypothesis [Tominaga and Stathopoulos, 2007]

$$- \langle u_i' c' \rangle = D_t \frac{\partial \langle C \rangle}{\partial x_i}. \tag{3}$$

where D_t is the turbulent mass diffusivity. The turbulent mass diffusivity is modeled as a ratio of turbulent momentum diffusivity (eddy viscosity) ν_t and turbulent Schmidt number Sc_t[Jischa and Rieke, 1979]:

$$- \langle u_i' c' \rangle = \frac{\nu_t}{Sc_t} \frac{\partial \langle C \rangle}{\partial x_i} \quad \text{with} \quad D_t = \frac{\nu_t}{Sc_t} \tag{4}$$

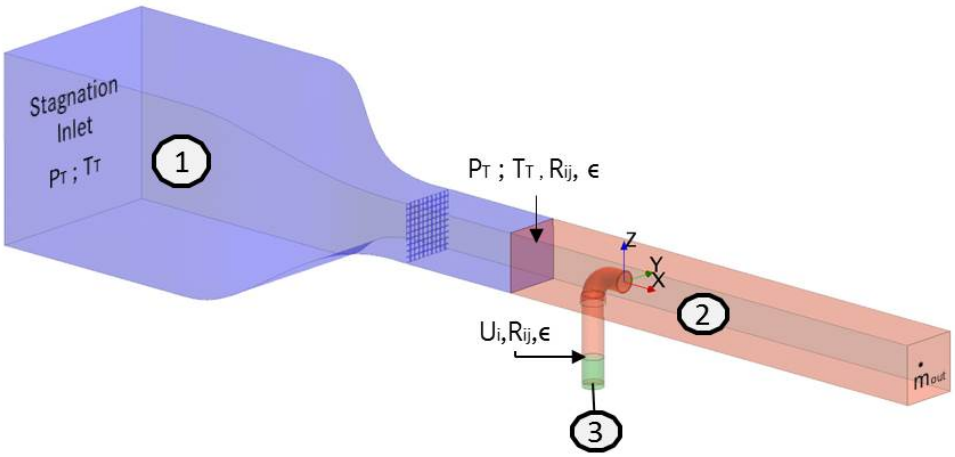

Fig. 8: The wind tunnel facility split into three parts: 1. plenum chamber and turbulence-generating grid, 2. mixing area, 3 periodic exhaust pipe

where $Sc_t = 0.9$. Due to high computational efforts simulating the complete flow facility the wind tunnel is split into three parts: the plenum chamber, the mixing area and the exhaust pipe, visualised in Fig. 8. A fully developed turbulent flow is assumed in the exhaust-gas supply pipe and was simulated separately in a short periodic pipe. The initialization based on the measured mass flow corresponds to hydraulic Reynolds number (see table 1). The velocity and turbulence distribution were used as the inlet condition for nozzle flow for all further simulation (see Fig. 8).
The outcome of the second pre-simulation provides the total pressure distribution and turbulence characteristics at the inlet section of the mixing area, which is considered to be far downstream from the turbulence-generating grid and the upstream impact of the nozzle pipe, as shown in Fig. 8. For this reason only the chamber and the wake behind turbulence grid were appropriate meshed, even so the full test facility was simulated, to predict the decay of homogeneous, isotropic turbulence after the flow passing through the turbulence-generating grid. According to the operation mode of the facility a stagnation inlet setup with ambient pressure was applied at the chamber entrance with a desired mass flow condition imposed at the outlet (see Fig. 8). The walls are assumed to be hydraulically smooth, which allows applying a non-slip condition $U_{wall} = 0$. In order to gain anisotropic turbulence behaviour all pre-calculations are solved using a Reynolds-stress model (RSM) [Speziale et al, 1990]. Finally, the imposed boundary conditions discussed above and application of the specified mass flow from table 1 as the outlet condition results in the velocity profiles of predicted data in front of the exhaust pipe, as shown in Fig. 9. Despite small oscillations in the wall normal velocity, the profiles are in good agreement with the measurements. A possible reason for these oscillations might be insufficient number of samples.

6.1 Computional mesh

For the present work, the core volume mesh is generated using the polyhedral cell type. The prism layers are inserted next to the wall to resolve the near wall gradients, as illustrated in Fig. 10.
In order to create a suitable wall resolved mesh, pre-calculations were performed to estimate the non-dimensional distance $y^+ = yu_\tau/\nu$ as a function of the friction velocity $u_\tau = (T_w/\rho)^{0.5}$, where T_w is the wall shear stress. According to the measured mass flows (see table 1) the wall shear stress is determined at different locations. All details of the grid and geometry parameters are listed in table 4. The total number of cells is 445000.

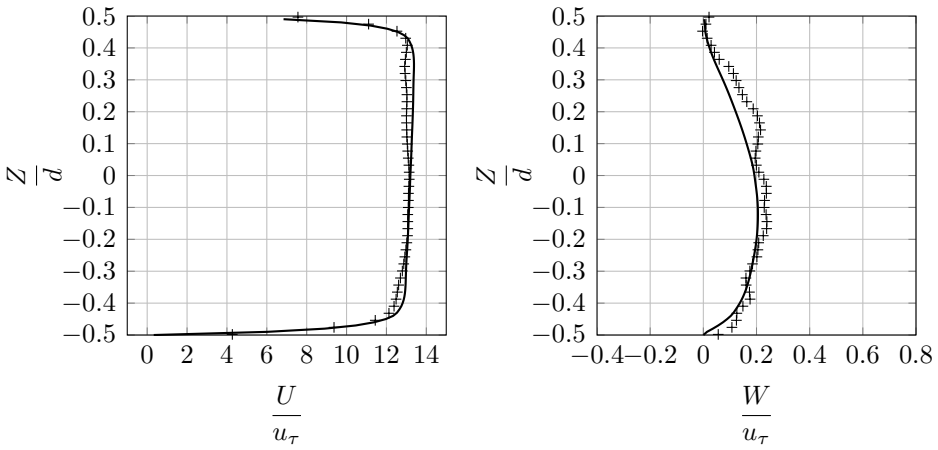

Fig. 9: Mean streamwise and normal wall velocity located at x=-120mm. Solid lines: RSM results, + measured data (N=500)

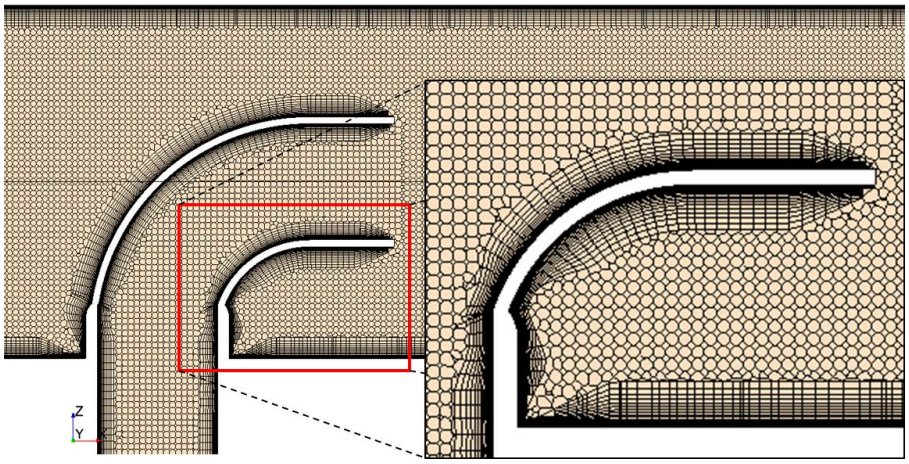

Fig. 10: The core volume meshed with polyhedral cell and the boundary layer is resolved by prism layers

Tab. 4: Grid and geometry parameters for the mixing area. The plane position gives the location of the different boundaries

	$Plane\ pos.[m]$	$U_{bulk}[m/s]$	Δ [m]	$\Delta_+(T_w)$	$y^+_{1.Cell}$
Inlet	$x = -0.15$	3.25	0.0013	15	0.5
Outlet	$x = \ 0.3$	4.905	0.0013	22.5	1
Exh. pipe	$z = -0.15$	19.55	0.0013	86.5	0.5

7. Results

7.1 Convergence of measured averages and fluctuations

The convergence of averages obtained from PIV and PLIF is evaluated by the absolute deviation $D_x = \overline{x_n} - \overline{x_N}$ of the component x with n being the number of samples and N being the number of maximum available samples. The convergence of fluctuations is assessed on the basis of the root-mean-square (RMS) of each component. All outliers and results from second order correlation peaks are excluded from velocity averaging (validation scheme provided in table 2). Two different pulse separations are tested, $\Delta t = 25\,\mu$s and $\Delta t = 35\,\mu$s.

Fluctuations of PLIF images due to photon/pixel noise are removed to some extent by a Gaussian low pass filter. Kernel sizes of the low pass filter are set to fractions of ¼ and ⅛ of the PIV interrogation window size. Thus, the spatial resolution of concentration fields is kept at a comparable level as for velocity measurements.

Results are evaluated in regions with the size matching a single PIV interrogation window in the upper and lower shear layer 10 mm downstream from the nozzle exit. These regions are most susceptible to PIV signal loss due to the presence of high shear stress. On the other hand the beginning entrainment in this area already leads to fluctuations of the concentration.

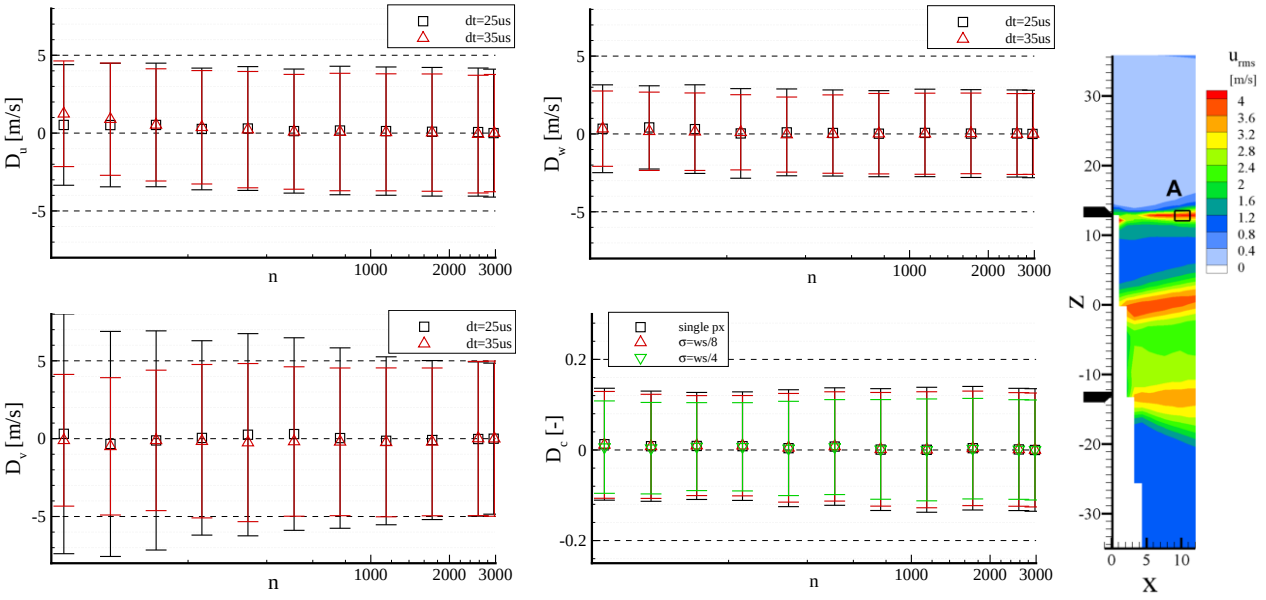

Fig. 11: Deviation from final average and standard deviation (RMS) over number of samples for a single PIV interrogation window placed in region A

Fig. 11 shows the results for the interrogation window A in the upper shear layer. Averages and standard deviation (RMS) of u, w and c show no significant deviation in the range of $2000...3000$ samples. The final standard deviations at $\Delta t = 35\,\mu$s is slightly lower which is probably due to increased loss of pairs. The standard deviation of the out-of-plane component v shows stronger fluctuations and converges slower which most likely is due to the higher uncertainty of out-of-plane measurements (see Fig. 3).

The convergence in region B (Fig. 12) shows a similar behaviour. Due to stronger out-of-plane components in the wake of the $90°$ bend and a increased loss of pairs the number of valid samples is decreased to 2000 at a pulse separation of $\Delta t = 35\,\mu$s. As one might expect, the standard deviation of the concentration in regions A and B decreases with increasing low pass filter kernel size. The extracted profiles provided for a comparison to CFD are low pass filtered with $\sigma = 0.25$ws.

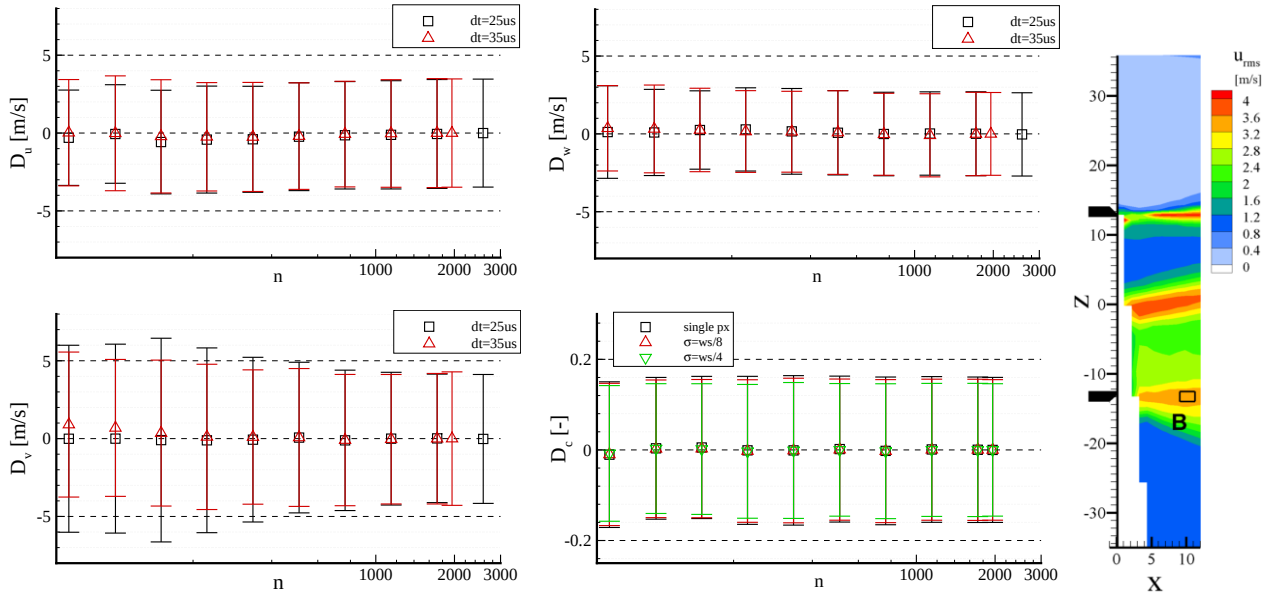

Fig. 12: Deviation from final average and rms over number of samples for a single PIV interrogation window placed in region B

7.2 Results of combined measurements

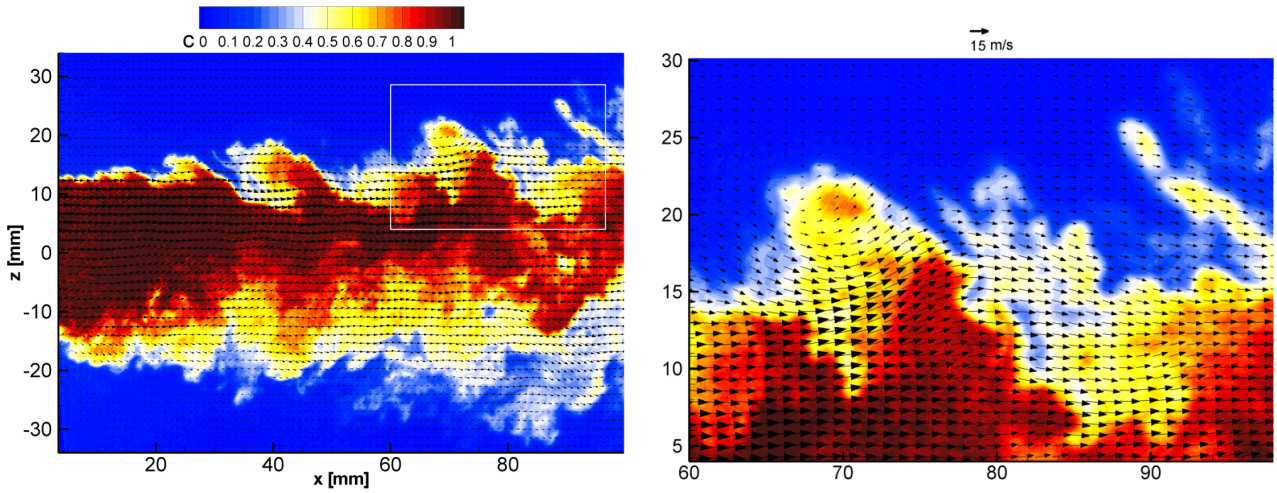

Fig. 13: Single shot of simultaneous velocity and concentration field, left: overview (skip=2 in z-direction), right enlarged region within the white box

The single shot of mixing fraction and velocity in Fig. 13 gives an impression of the turbulent character of the flow. Large vortices in the upper shear layer indicates large scale mixing. These vortices break up into small-scale velocity fluctuations which accelerate the mixing and diffusion. Faster mixing and diffusion occurs in the lower area of the jet possibly due to the radial pressure gradient at the 90° bend exit causing ambient air to be sucked in. Another reason for a faster mixing on the lower side might be the wake of the bent which induces additional out-of-plane motion.
Fig. 14 shows the ensemble averaged axial velocity and concentration. The maximum axial velocity at 22 m/s appears near the upper side (outside wall) of the bend. The jet potential core is deformed towards the upper region with the higher momentum fluid remaining unmixed the longest. The isolines of velocity and mixing fraction are convex curved on the lower side of the 90° bend while they start almost linear at the upper shear layer. Isolines of mixing fraction at $c = 0.1$ and $c = 0.2$ are concave

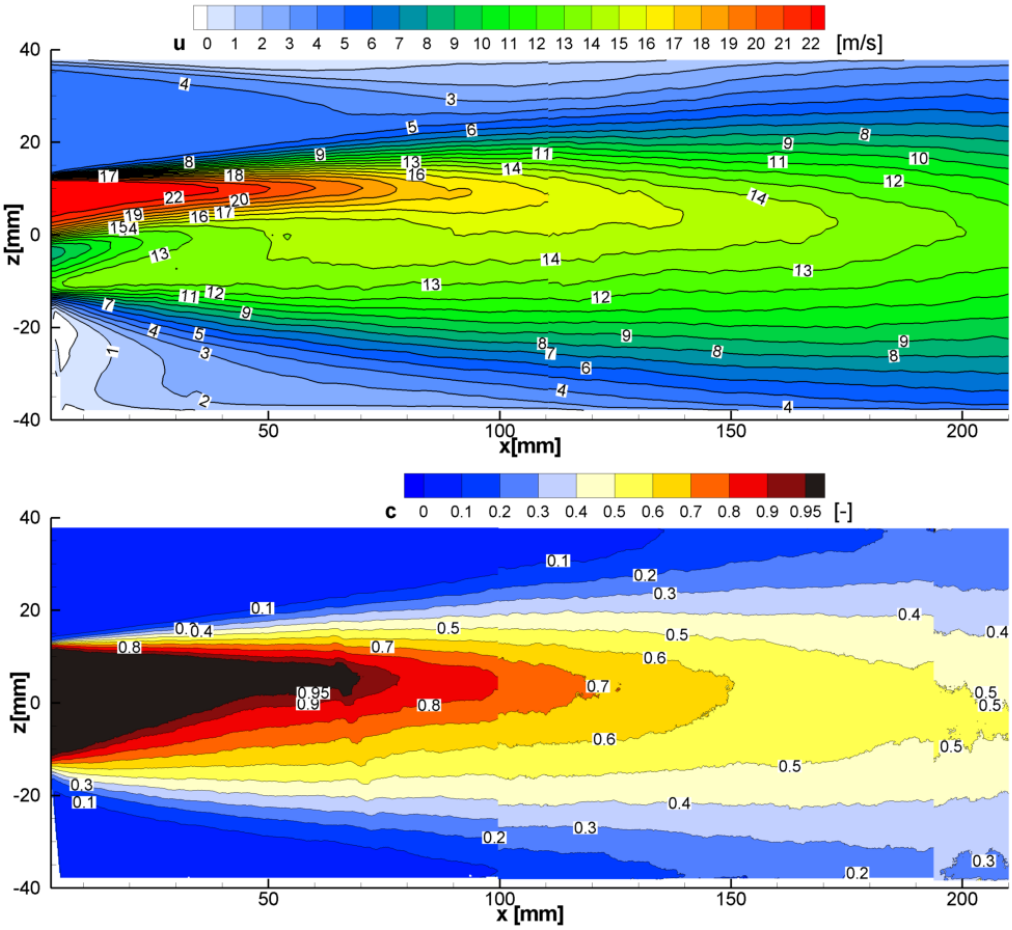

Fig. 14: Average of axial velocity component and of mixing fraction (N=500)

near the upper wall which is not the case at the lower wall.

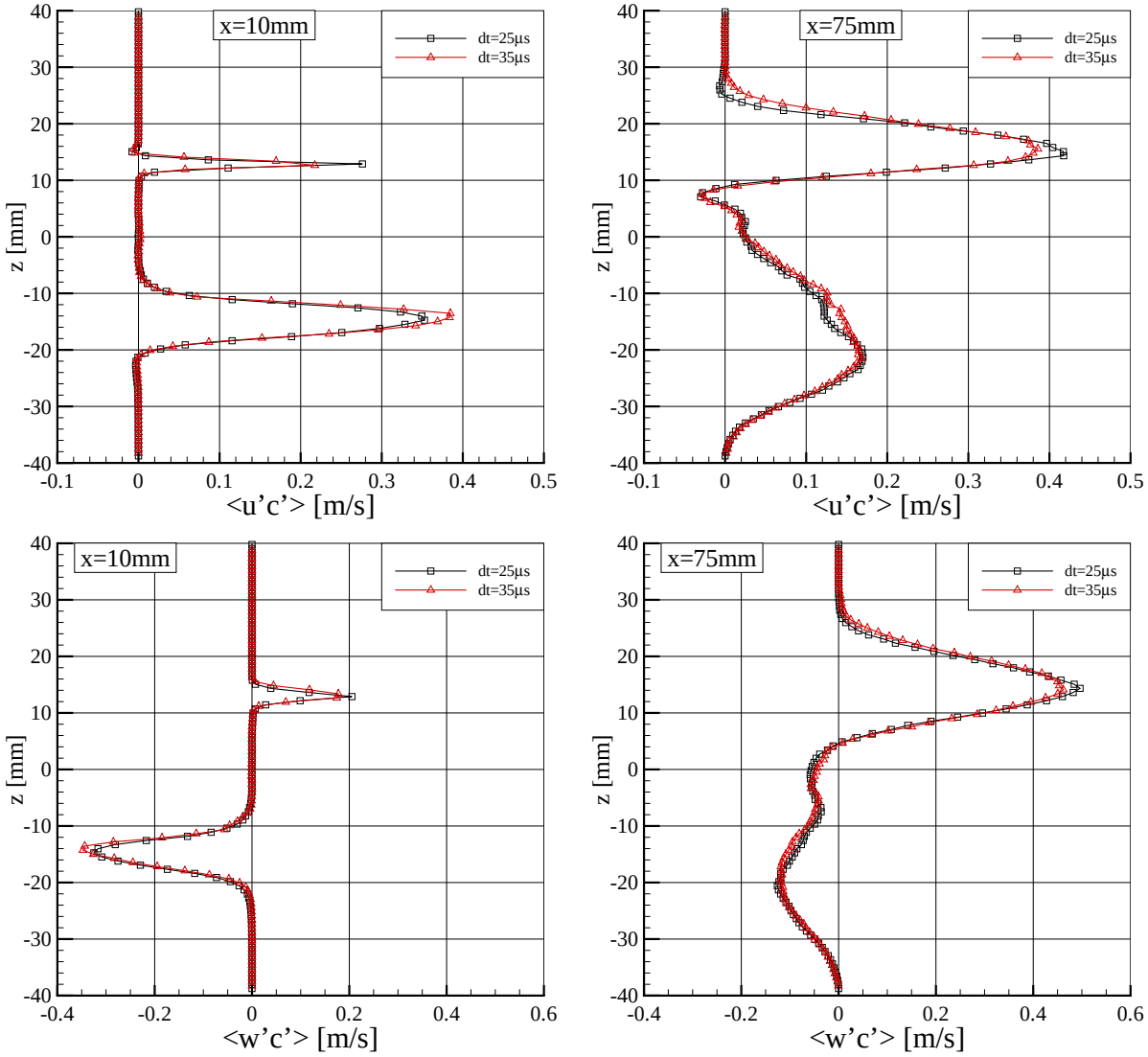

Fig. 15: Time averaged turbulent mass flux $\langle u'c' \rangle$ (top) and $\langle w'c' \rangle$ (bottom) at distances of x=0.4d and x=3d and two PIV pulse separations

The turbulent mass fluxes are obtained from the covariances of velocity and mixing fraction from the long sequences. Fig. 15 shows vertical profiles at $x = 0.4d$ and $x = 3.0d$. The streamwise turbulent mass flux $\langle u'c' \rangle$ has a symmetric orientation while the wall normal flux $\langle w'c' \rangle$ has a antisymmetric orientation with respect to the tunnel's centerline. At $x = 0.4d$ covariances $\langle u'c' \rangle$ and $\langle w'c' \rangle$ have stronger magnitudes in the shear layer above the centerline than below the centerline. Near the jet exit the streamwise turbulent mass flux is larger than the wall normal mass flux. Further downstream at $x = 3.0d$ the turbulent mass flux (and turbulent diffusion) grow more strongly in the upper shear layer while it spreads along the z axis in the lower shear layer. The $\langle u'c' \rangle$ distribution at $x = 3.0d$ shows some oscillations between $z = -30..0\,\mathrm{mm}$. Possibly, in that region a sample count of $N = 3600$ might still be insufficient to achieve statistical convergence.

7.3 Results of the comparison to numerical results

The region of interest is simulated with three fundamental turbulence models, the $k - \epsilon$ [Shih et al, 1995] realizable model with curvature correction (KE) [Arolla and Durbin, 2013], the shear-stress-transport $k - \omega$ model (SST) [Menter, 1994] and the Reynolds-stress model [Speziale et al, 1990].

More detailed discussion of all three models can be found in Refs. [Shih et al, 1995; Menter, 1994; Speziale et al, 1990]. All computed results are evaluated along vertical lines located in the measured plane at four different downstream locations in the mixing area.

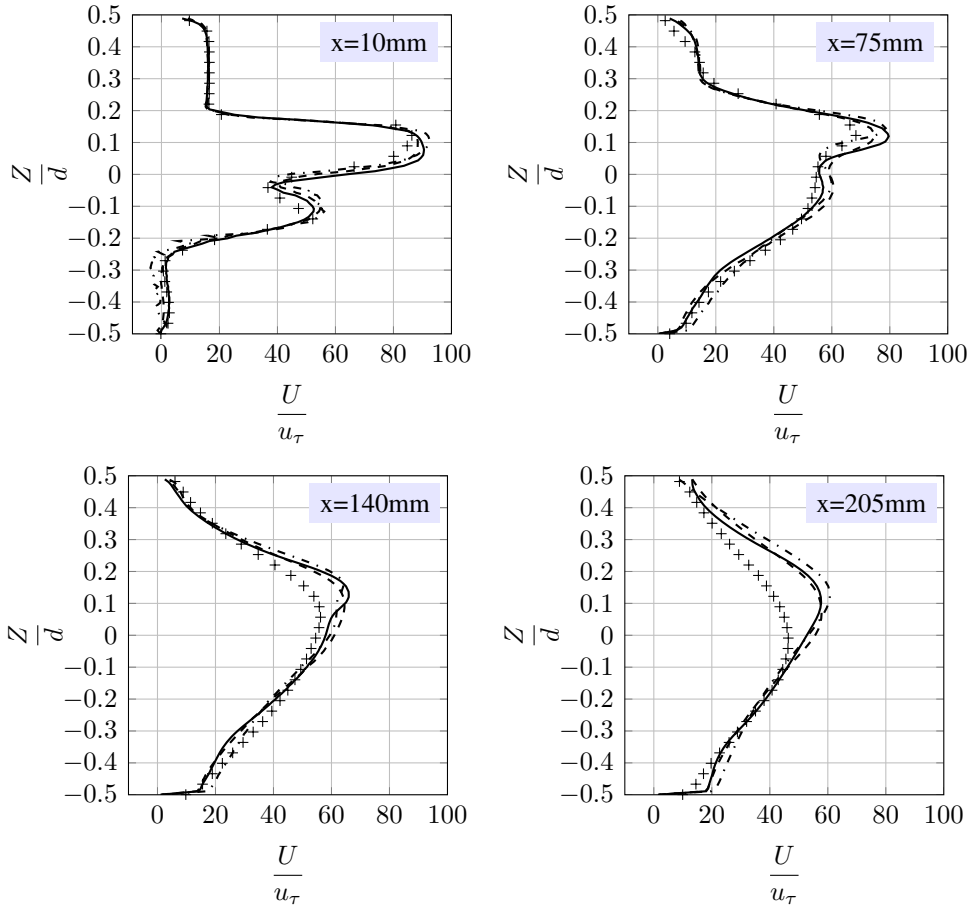

Fig. 16: Mean streamwise velocity at different downstream location in the mixing area. Solid lines: RSM results, dash-dotted lines: k-ω results,dashed lines: k-ϵ results, + measured data

Fig. 16 shows the velocity profiles normalized by the friction velocity at the outlet (see in table 1). The results obtained by STARCCM+ are in good agreement with the experimental data at $x = 0.01$ m, which is shortly behind the nozzle exit. With increasing distance from the injection point, the differences between measured and calculated data increase slightly, although the characteristic curve shape is preserved. The calculated wall normal velocity distribution shows quantitatively and qualitatively higher variation as the streamwise velocity, as visualized in Fig. 17. A reason for this numerical deviation may lie in insufficient modelling of shear stress in wall bounded flows.
The mass fraction, as presented in Fig. 18, is determined by solving the mass transport equation (Equation 2), whereby the "standard" gradient hypothesis is used to obtain turbulent mass flux $\langle u'c' \rangle$. Obviously, the simulated potential core of the nozzle jet is convected a greater distance downstream. This behaviour identifies a significant trend towards the underestimation of the mixing processes, especially the sharp transition (to the lower level of the mass fraction) in the wall normal direction indicates insufficient diffusion. Due to the fact that the simulated velocity field is not identical with experimental data, the advective mass transport is slightly impaired by the convective term (Equation 2).
Aside from the convective transport the turbulent diffusion mainly influences the prediction of the mixing processes. As mentioned above, the turbulent diffusion is described by $\langle u'c' \rangle$ and shown in Fig. 19 and Fig. Fig. 20 normalised by outlet friction velocity. It is evident that the gradient transport

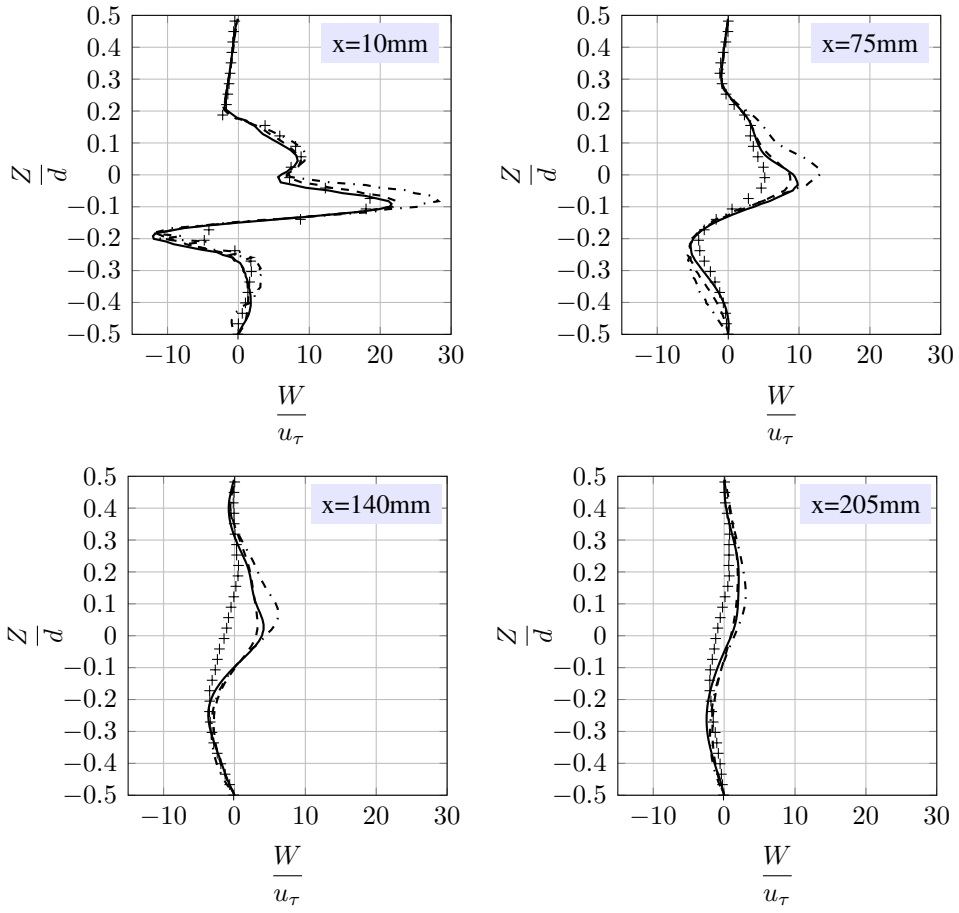

Fig. 17: Mean wall normal velocity at different downstream location in the mixing area. Solid lines: RSM results, dash-dotted lines: k-ω results,dashed lines: k-ϵ results, + measured data

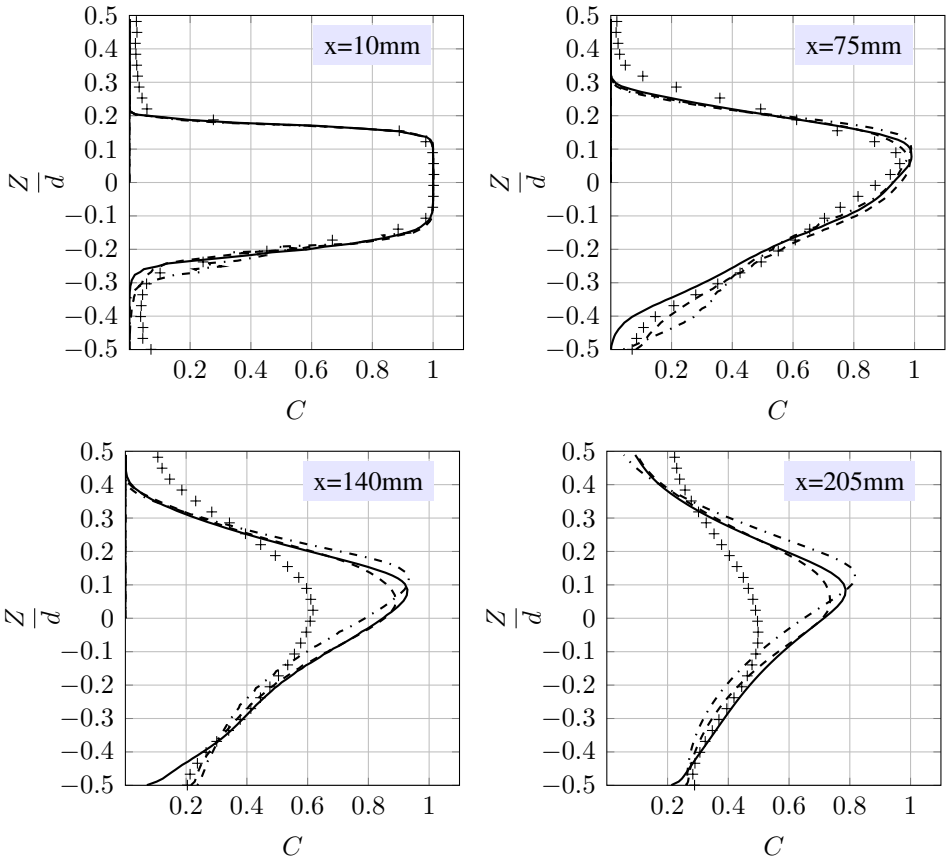

Fig. 18: Mean concentration at different downstream location in the mixing area. Solid lines: RSM results, dash-dotted lines: k-ω results,dashed lines: k-ϵ results, + measured data

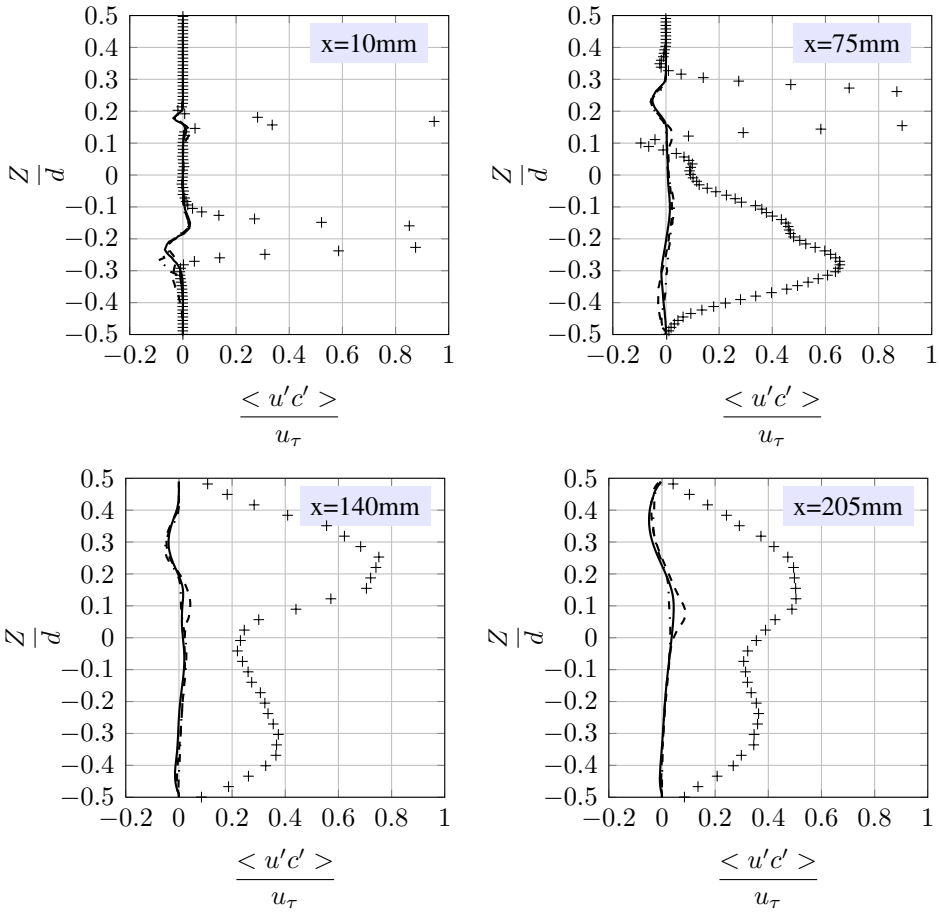

Fig. 19: Mean streamwise turbulent mass flux at different downstream location in the mixing area. Solid lines: RSM results, dash-dotted lines: k-ω results,dashed lines: k-ϵ results, + measured data

model (Equation 4) are unable to capture the streamwise turbulent mass flux either quantitatively or qualitatively. However, the characteristic profile of the calculated wall normal mass flux shows better agreement with the experimental data. The main reason for this deviation lies in the isotropic formulation of the turbulent mass flux model, which is not able to cover anisotropic turbulence behaviour forced by dominated shear flow, as often discussed in the literature [Suga and Abe, 2000; Daly and Harlow, 1970].

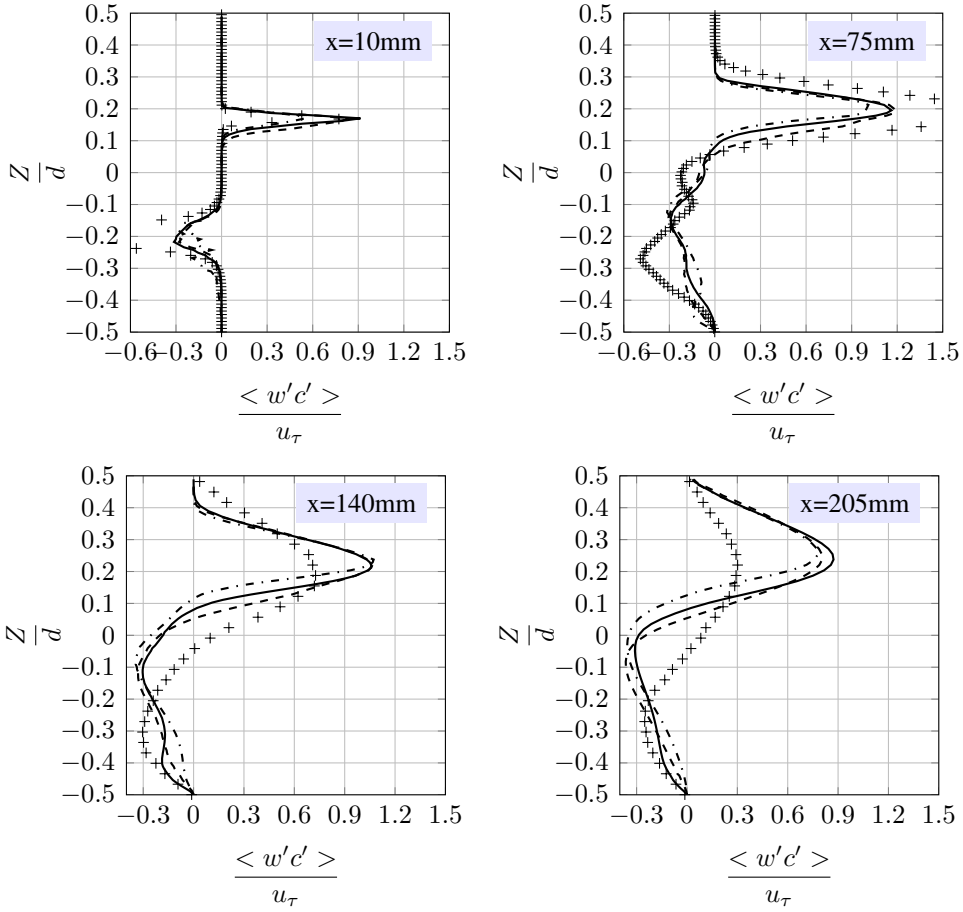

Fig. 20: Mean wall normal turbulent mass flux at different downstream location in the mixing area. Solid lines: RSM results, dash-dotted lines: k-ω results,dashed lines: k-ϵ results, + measured data

8. Conclusions and Outlook

A combined PLIF and stereo PIV system was developed to simultaneously measure mass fraction and velocity in the isothermal mixing zone of a confined coaxial jet in air. Sets of up to 3600 measurements are used to extract vertical profiles of mean velocity, concentration and turbulent mass fluxes at four downstream positions with respect to jet exit. The convergence of fluctuations is assessed by plotting the root-mean square of velocity components and mixing fraction over N at two exemplary positions of PIV interrogation windows in the shear layers. The fluctuations were found to show no significant variations after $2000..3000$ samples. The out-of-plane component converges slower than the in plane components and finally has higher fluctuations, probably due to the lower measurement accuracy.
Extracted profiles of ensemble averaged in-plane velocities, mass fraction and turbulent mass fluxes are compared to RANS and Reynolds averaged mass transport simulations. The comparison of experimental and numerical data shows, that the statistics of the RANS prediction strongly underestimates the degree of mixing and diffusion which in part may be attributed to the anisotropic behavior of the

turbulent flow. The main reason for this deviation lies in the isotropic formulation of the turbulent mass flux model, which is not able to cover anisotropic turbulence behaviour forced by dominated shear flow. Therefore experimental results presented here contribute to the development and validation of new turbulence models with improved prediction of mass fraction.

Acknowledgements

The authors would like to thank Manfred Beversdorff for his help during construction of the windtunnel and Wolfgang Förster for the programming of data acquisition system.

References

Arolla SK, Durbin PA (2013) Modeling rotation and curvature effects within scalar eddy viscosity model framework. International Journal of Heat and Fluid Flow 39(0):78 – 89, DOI http://dx.doi.org/10.1016/j.ijheatfluidflow.2012.11.006, URL http://www.sciencedirect.com/science/article/pii/S0142727X12001427

Bryant RA, Donbar JM, Driscoll JF (2000) Acetone laser induced fluorescence for low pressure/low temperature flow visualization. Experiments in Fluids 28(5):471–476, DOI 10.1007/s003480050407, URL http://dx.doi.org/10.1007/s003480050407

Coppeta J, Rogers C (1998) Dual emission laser induced fluorescence for direct planar scalar behavior measurements. Experiments in Fluids 25(1):1–15, DOI 10.1007/s003480050202, URL http://dx.doi.org/10.1007/s003480050202

Daly BJ, Harlow FH (1970) Transport equations in turbulence. Physics of Fluids (1958-1988) 13(11):2634–2649, DOI http://dx.doi.org/10.1063/1.1692845, URL http://scitation.aip.org/content/aip/journal/pof1/13/11/10.1063/1.1692845

Fox RO (2003) Computational Models for Turbulent Reacting Flows. Cambridge University Press, URL http://dx.doi.org/10.1017/CBO9780511610103

Heinze J, Meier U, Behrendt T, Willert C, Geigle K, Lammel O, Lückerath (2011) Plif thermometry based on measurements of absolute concentrations of the oh radical. International journal of research in physical chemistry and chemical physics 225(11–12):1315–1341, DOI 10.1524/zpch.2011.0168

Jischa M, Rieke HB (1979) About the prediction of turbulent prandtl and schmidt numbers from modeled transport equations. International Journal of Heat and Mass Transfer 22(11):1547 – 1555, DOI http://dx.doi.org/10.1016/0017-9310(79)90134-0, URL http://www.sciencedirect.com/science/article/pii/0017931079901340

Lozano A, Yip B, Hanson R (1992) Acetone: a tracer for concentration measurements in gaseous flows by planar laser-induced fluorescence. Experiments in Fluids 13(6):369–376, DOI 10.1007/BF00223244, URL http://dx.doi.org/10.1007/BF00223244

Menter FR (1994) Two-equation eddy-viscosity turbulence models for engineering applications. AIAA Journal 32(8):1598–1605, DOI 10.2514/3.12149, URL http://dx.doi.org/10.2514/3.12149

Prasad AK (2000) Stereoscopic particle image velocimetry. Experiments in Fluids 29(2):103–116, DOI 10.1007/s003480000143, URL http://dx.doi.org/10.1007/s003480000143

Raffel M, Willert C, Wereley S, Kompenhans J (2007) Particle Image Velocimetry, A Practical Guide. Springer Berlin-Heidelberg

Shih T, Liou W, Shabbir A, Yang Z, Zhu J (1995) A new k-epsilon eddy viscosity model for high reynolds number turbulent flows. Computers and Fluids URL http://www.ingentaconnect.com/content/els/00457930/1995/00000024/00000003/art00032

Speziale CG, Sarkar S, Gatski TB, Center LR (1990) Modeling the pressure-strain correlation of turbulence [microform] : an invariant dynamical systems approach / Charles G. Speziale, Sutanu Sarkar, Thomas B. Gatski. National Aeronautics and Space Administration, Langley Research Center Hampton, Va

Starccm (2013) User Guide

Suga K, Abe K (2000) Nonlinear eddy viscosity modelling for turbulence and heat transfer near wall and shear-free boundaries. International Journal of Heat and Fluid Flow 21(1):37 – 48, DOI http://dx.doi.org/10.1016/S0142-727X(99)00060-0, URL http://www.sciencedirect.com/science/article/pii/S0142727X99000600

Thurber MC, Grisch F, Kirby BJ, Votsmeier M, Hanson RK (1998) Measurements and modeling of acetone laser-induced fluorescence with implications for temperature-imaging diagnostics. Appl Opt 37(21):4963–4978, DOI 10.1364/AO.37.004963, URL http://ao.osa.org/abstract.cfm?URI=ao-37-21-4963

Tominaga Y, Stathopoulos T (2007) Turbulent schmidt numbers for {CFD} analysis with various types of flowfield. Atmospheric Environment 41(37):8091 – 8099, DOI http://dx.doi.org/10.1016/j.atmosenv.2007.06.054, URL http://www.sciencedirect.com/science/article/pii/S1352231007006036

Tran T, Kochar Y, Seitzman J (2005) Measurements of liquid acetone fluorescence and phosphorescence for two-phase fuel imaging. In: 43rd Aerospace Sciences Meeting and Exhibit, Reno (NV), AIAA-2005-0827

Willert C (submitted) High-speed particle image velocimetry for the efficient measurement of turbulence statistics. Exp Fluids